Journal of
Materials Chemistry A

ROYAL SOCIETY OF CHEMISTRY

PAPER

View Article Online
View Journal | View Issue

Cite this: *J. Mater. Chem. A*, 2022, **10**, 13839

Atomic step formation on porous ZnO nanobelts: remarkable promotion of acetone gas detection up to the parts per trillion level†

Kyusung Kim, Pil gyu Choi, Toshio Itoh and Yoshitake Masuda *

Received 6th April 2022
Accepted 3rd June 2022

DOI: 10.1039/d2ta02789e

rsc.li/materials-a

Atomic defects, such as steps and kinks, can promote the efficiency of chemical reactions. These defects provide coordinatively unsaturated sites (CUSs) in metal oxides and the CUSs react with other molecules with relatively lower energy. Thus, decoration with atomic step structures can be a cost-effective strategy that can replace novel metal catalysts to enhance the gas sensing performance. Herein, atomic step structure decorated porous ZnO nanobelts were synthesized for acetone gas sensing below the parts-per-trillion (ppt, 10^{-12}) level. Numerous atomic step structures could be formed by removing H and F atoms that occupied a high atomic ratio and a low weight ratio, during the conversion process of ZnOHF. Atomic step structures on ZnO allow an outstanding sensitivity, *i.e.*, detection up to 200 ppt, and its theoretical limit of detection (LOD) was 72 ppt. This result was due to the edge of the atomic step that promotes electron transfer and induces oxygen chemisorption by restricting the diffusion on the flat surface. The atomic defect engineering on the metal oxide by conversion from metal hydroxide fluoride will trigger the fabrication of extremely sensitive sensing materials that do not require novel metal catalysts.

1. Introduction

Controlling the exposed crystal facet is a well-known effective strategy for enhancing the reactivity of nanomaterials without using expensive catalysts, such as Pt, Pd, and Ru.[1–4] Following this strategy, the morphology of nanomaterials has been varied by controlling the growth direction, and the suitable facets for desired reactions have been investigated. However, atomic level surface modification could provide a considerably higher surface reactivity. This modification method forms kink and step structures representative of atomic defects on the surface. The coordination numbers of the atoms located at the steps and kinks are lower than those of other atoms. Thus, chemical reactions preferentially occur at these positions.[5–8] These coordinatively unsaturated sites have been investigated to improve the chemical reaction efficiency. For instance, the reactivities for dehydrogenation on Pt and N_2 activation on Ru were enhanced at step structures.[9–11] Moreover, steps are equivalent to the existence of various types of crystal facets within a single specific facet. Consequently, the reaction efficiency of the exposed facet can be dramatically improved by atomic level modification. Therefore, nanomaterials modified using this technique can be applied for ultrasensitive gas sensing.

Volatile organic compound (VOC) analysis of skin gas is an attractive technique for advanced healthcare applications. VOCs, such as acetone, ammonia, and nitric oxide, are byproducts of human physiology that have been investigated because their composition and concentration are potential indicators of health conditions.[12–14] In particular, acetone is formed *via* ketonization through metabolism or lipolysis, and its concentration can provide important information about the body.[15] In general, the VOC analysis technique is a noninvasive and convenient method, which has been performed using human breath.[15,16] Owing to the recent development of wearable materials, skin gas analysis is desired because of its outstanding ability to collect information in real time for a long period.[17–21] However, sensors for skin gas require superior sensitivity compared with that of breath gas sensors. For example, the acetone concentration in the exhaled breath of a patient with diabetes is over 1.8 ppm,[22] whereas the acetone concentration in skin gas is a few tens of parts per billion (ppb) in the reference model and a few hundred ppb for patients with diabetes.[23,24] In addition, a diagnosis based on the specific standard concentration is not reasonable owing to differences between individuals. Thus, continuous monitoring of the variation in the acetone concentration is more suitable for a comprehensive assessment of health conditions. To detect small variations in the acetone concentration in skin gas, the development of sensor materials that are reliable not only at the ppb level but also at the parts-per-trillion (ppt) level is required.

In this study, porous ZnO nanobelts with atomic step structures were prepared for ppt-level gas sensing. The morphology and formation process of the atomic step structure on the ZnO surface were investigated. For sensing applications,

---

Institute of Advanced Industrial Science and Technology (AIST), 2266-98 Anagahora, Shimoshidami, Moriyama, Nagoya 463-8560, Japan. E-mail: masuda-y@aist.go.jp

† Electronic supplementary information (ESI) available. See https://doi.org/10.1039/d2ta02789e

the gas sensitivity and selectivity were confirmed under optimized conditions. In particular, the linearity of the gas response for acetone concentration below ppb and ppt levels was evaluated for sensor reliability.

2. Results

2.1. Material characterization

A schematic of the formation process of the porous ZnO nanobelts is presented in Fig. 1a. ZnOHF nanobelts were synthesized after the reaction of $ZnF_2 \cdot 4H_2O$ and hexamethylenetetramine (HMT) at 80 °C. The ZnOHF nanobelts were converted into porous ZnO nanobelts with atomic steps by heat treatment at 500 °C for 2 h. The white powder, ZnOHF, changed to light yellow during this process (Fig. S1†), which may indicate the presence of numerous oxygen vacancies in the ZnO structure. To clarify the conversion temperature from ZnOHF to ZnO, thermogravimetric analysis (TGA) of ZnOHF was performed up to 900 °C in air. In total, 25% weight loss occurred during the process, as shown in Fig. 1b. The initial approximately 5%

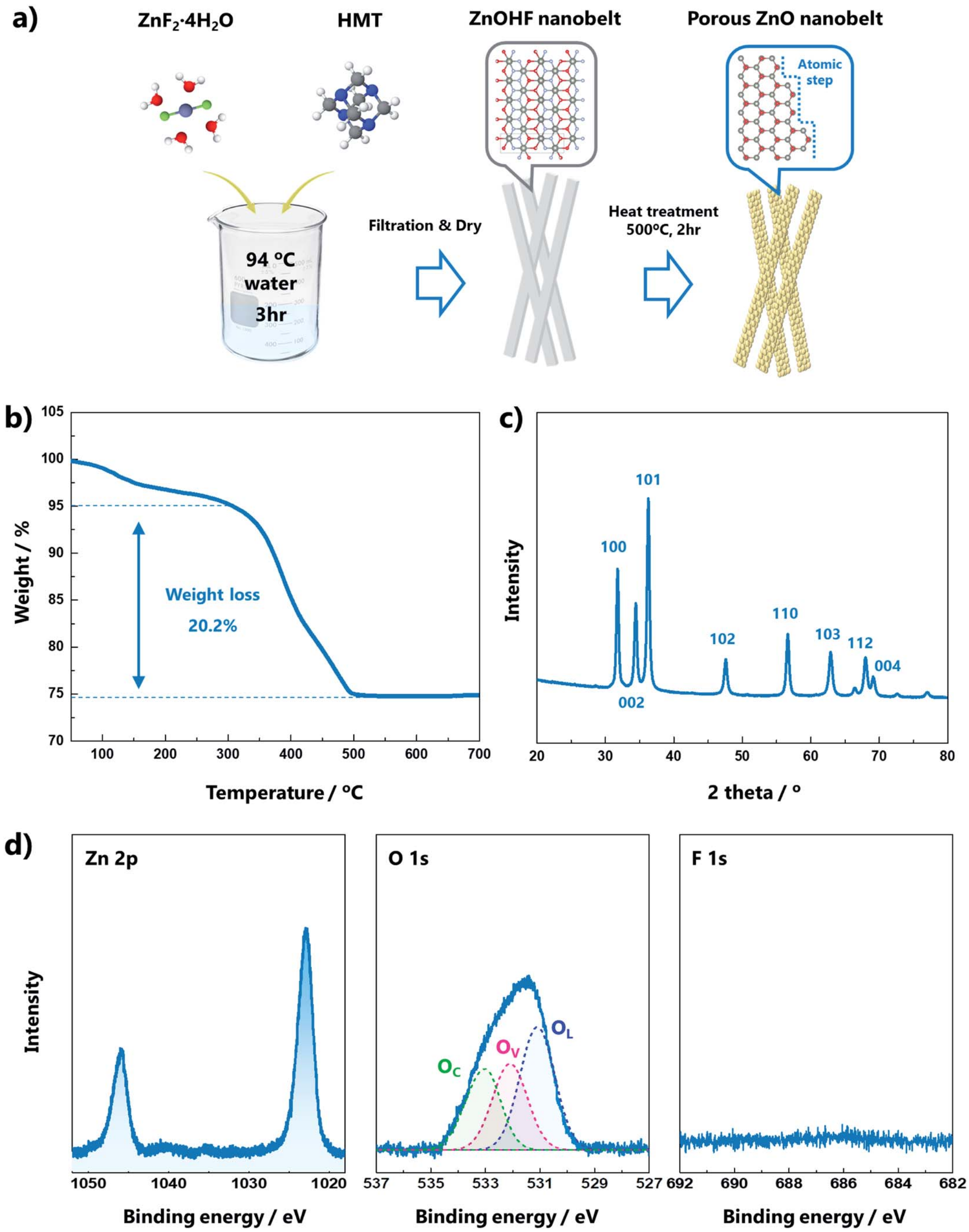

Fig. 1 (a) Schematic of the synthesis process of porous ZnO nanobelts by conversion of ZnOHF; (b) TGA curves of the ZnOHF structure with weight loss from moisture and HF; and (c) XRD pattern and (d) high-resolution Zn 2p, O 1s, and F 1s XPS spectra of the porous ZnO nanobelts.

weight loss is attributed to the removal of adsorbed water. Subsequently, the weight of ZnOHF rapidly decreased (20% weight loss) from 320 to 490 °C. This weight loss indicates the decomposition of ZnOHF into ZnO and HF, and the ratio of weight loss is consistent with the atomic weight ratio (relative atomic weights, Zn: 65, O: 16, H: 1, F: 19).[25]

X-ray diffraction (XRD) analysis was conducted to confirm the crystalline structures of the samples. The diffraction pattern of the ZnO nanobelts (Fig. 1c) was indexed to the hexagonal wurtzite structure $P6_3mc$ (JCPDS no. 36-1451), indicating complete conversion to the ZnO structure after calcination at 500 °C when compared with the XRD pattern of ZnOHF (Fig. S2a†). X-ray photoelectron spectroscopy (XPS) analysis was conducted to determine the chemical bonding information (Fig. 1d). In the high-resolution Zn 2p spectrum, two peaks associated with $2p_{3/2}$ and $2p_{1/2}$ were observed at 1022.6 and 1045.7 eV, respectively. The O 1s spectrum was deconvoluted into three Gaussian distributions, located at 531.11, 532.13, and 533.03 eV. The peak at 531.11 eV was attributed to O^{2-} ions in the lattice (O_L), the peak at 531.13 eV was assigned to oxygen vacancies (O_V), and the peak at 533.03 eV was ascribed to the O chemisorbed state of dissociated oxygen (O_C).[26] The O_C can influence the gas-sensing performance because the pre-adsorbed O species are a significant component that reacts with target gas molecules.[27] The area proportion of each peak in the O 1s spectrum is presented in Table S1.† The peak associated with F 1s was not observed because the HF disappeared during heat treatment. Compared with the XPS results of ZnOHF (Fig. S2b†), the differences in the peaks prove the complete conversion to ZnO. The Zn 2p peaks were slightly blue-shifted (2.4 eV), indicating considerable oxygen deficiency in ZnO. The dominant OH peak in the O 1s spectrum and the strong F 1s peak for ZnOHF were no longer observed. The specific surface areas of the nanobelt structures were characterized by N_2 adsorption/desorption isotherms. As presented in Fig. S2c,† the calculated Brunauer–Emmett–Teller (BET) surface areas of the ZnO and ZnOHF nanobelts were 315.28 and 230.96 $m^2\ g^{-1}$, respectively. The BET value increased because the conversion of ZnOHF into ZnO led to the formation of a porous structure.

Field-emission scanning electron microscopy (FE-SEM) was used to examine the morphologies of the ZnO nanobelts. As shown in Fig. 2a, there were numerous nanobelt structures over the length of a few micrometers, which were thin enough that other structures were visible through them. The width of the nanobelts was less than 100 nm, and they appeared to have pores, as shown in Fig. 2b. The ZnOHF morphology was almost the same as that of ZnO, except that it lacked pores (Fig. S3a and b†). The porous structure of the ZnO nanobelts was clearly visible in the transmission electron microscopy (TEM) image in contrast to ZnOHF (Fig. 2c and S3c†). A detailed chemical analysis was conducted using high-angle annular dark-field (HAADF) scanning transmission electron microscopy (STEM) and energy-dispersive spectroscopy elemental mapping. The porous structure of ZnO was also confirmed by the presence of dark contrast regions, which were absent for ZnOHF (Fig. 2d and S3d†). In the elemental maps, Zn (49.5%) and O (50.2%) were uniformly distributed in ZnO, whereas Zn, O, and F existed at almost a 1 : 1 : 1 ratio in ZnOHF (Fig. 2e–g and S3e–g†).

Fig. S4a and b† show that ZnOHF grew continuously along the *b*-axis, and the growth orientation of ZnOHF was the ⟨010⟩ direction according to the corresponding selected area electron diffraction (SAED) pattern. As shown in Fig. 3a, each ZnO nanobelt appeared to be elongated along the growth direction of the ZnOHF structure rather than be spherical particles. The atomic step structures on the surface were clearly confirmed in the HR-TEM images. The step structures were distributed along the side of ZnO (Fig. 3b) and had various sizes (Fig. 3c). The

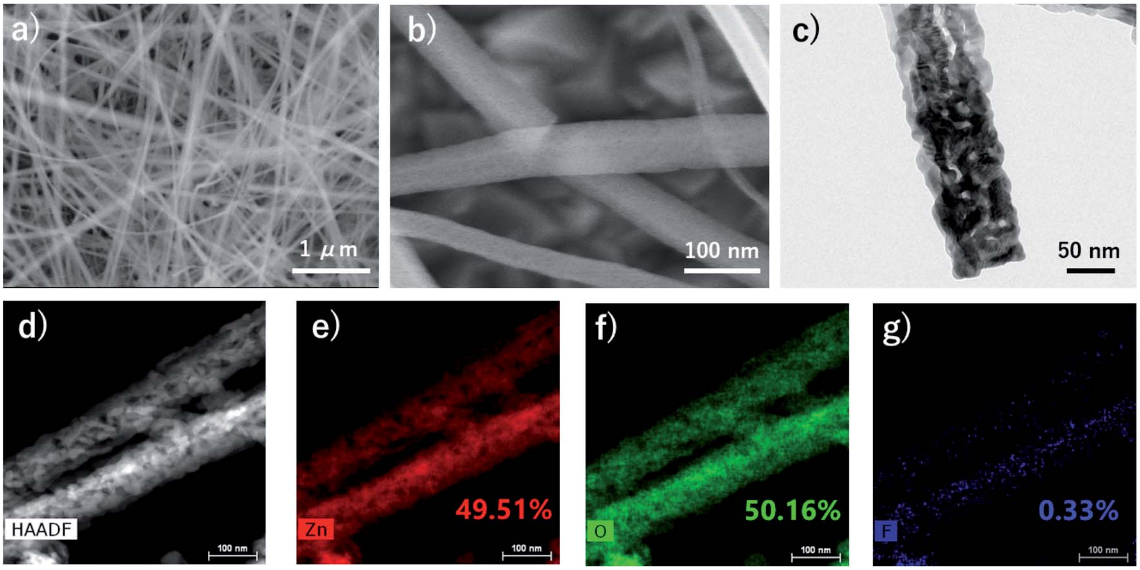

Fig. 2 (a) Low- and (b) high-magnification SEM images; (c) TEM image; (d) HAADF-STEM image; and (e) Zn, (f) O, and (g) F elemental maps of the porous ZnO nanobelts.

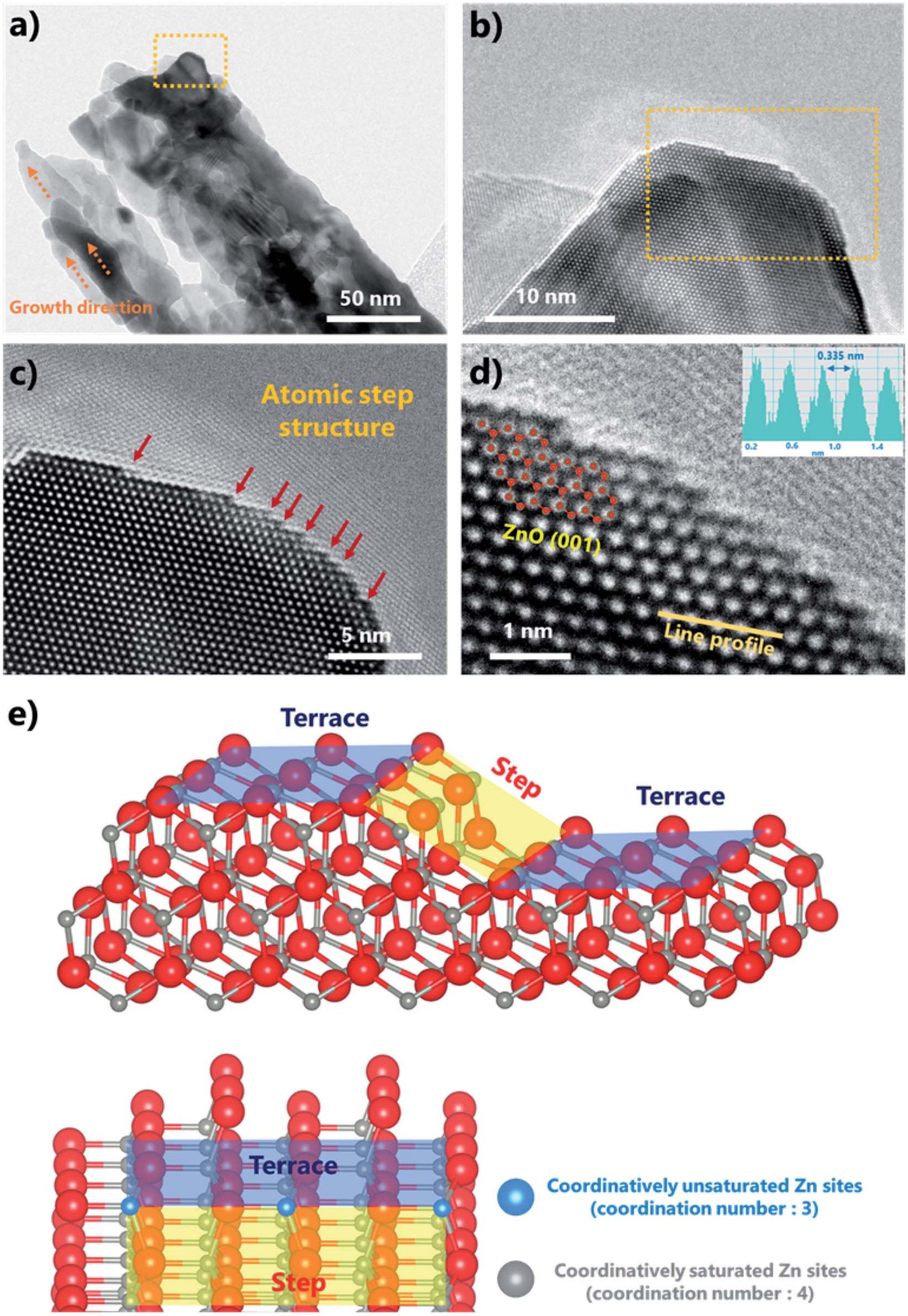

Fig. 3 (a) TEM image and (b–d) HR-TEM images of the atomic step structures at different magnifications, and (e) crystallographic schematics of the atomic step and terrace structures.

atomic step structures were not concentrated in a specific region but were distributed along the entire surface (Fig. S5a–d†). Porous nanobelts with elongated particles and atomic step structures formed because of the ZnOHF structure of the starting material. As shown in Fig. S6a and b,† Zn and O exhibited an elongated line morphology along the *b*-axis when the H and F in ZnOHF disappeared. The distances between Zn and O after H and F removal (Fig. S6c and d†) were the same or longer than the distance of typical ZnO (1.95 and 2.04 Å). Based on the TGA result, the weight did not increase after heat treatment in air; thus, additional oxygen was not supplied for the formation of ZnO. Consequently, the ZnO structure was built by the distortion of existing atoms in the structure due to the lack of O atoms. However, ZnO maintained the nanobelt structure of ZnOHF, as shown in the SEM results. Thus, this conversion process might have formed the porous structure and the atomic step structure on the surface. The line-scanning intensity profiles (inset in Fig. 3d) further revealed that the observed top facet was the (001) plane of ZnO with a 0.335 nm lattice spacing. Thus, the side exposed facet was (100) ZnO. The step length was not constant, but the step height was almost exactly the size of one atom. Depending on the terrace length, the step structure comprised various types of exposed facets, such as (20), (40), and (60), as shown in Fig. S7.† Furthermore, coordinatively unsaturated atoms were located at the edge of the atomic step, as shown in Fig. 3e. Typically, one Zn atom is coordinated with four O atoms in the ZnO structure. However, Zn atoms located at step edges are only connected to three O atoms. These coordinatively unsaturated metal sites received further attention owing to their enhanced catalytic effect due to facile electron transfer.[28–30]

2.2. Acetone gas detection performance

We investigated the gas-sensing performance to confirm the advantage of the atomic step structures in the ZnO nanobelts. The preparation of the gas sensor is shown in Fig. 4a. A dispersion of ZnO nanobelts was dropped and dried on a 3 × 3 mm substrate, which was assembled as a sensor. The stacked thickness of the ZnO nanobelt varies from 1 to 1.76 μm as shown in Fig. S8.† The dynamic equilibrium of gas adsorption and desorption on the oxide surface can be determined by the operating temperature. Thus, to find the optimal temperature for acetone gas sensing, the variation in the sensor temperature with the applied voltage was measured using a thermal distribution image (Fig. S9a†). At 500 ppb of acetone, the gas response was confirmed in the range 425–525 °C, and the maximum response value (15.9) was obtained at 450 °C, as shown in Fig. S9b.† The response and recovery times of the porous ZnO nanobelts were 20 and 240 s, respectively (Fig. S9c†). The response time (τ_{res}) is defined as the time required for the response to reach 90% of the maximum value from immediate target gas exposure, and the recovery time (τ_{rec}) is defined as the time required for the response value to reach 10% of the minimum value after exposure to air. In addition, the short- and long-term stabilities of the gas sensor were confirmed as presented in Fig. S10.† The gas selectivity for acetone was confirmed by measuring isoprene, toluene, ammonia, nitrogen dioxide, and hydrogen gases at 500 ppb, as shown in Fig. 4b. The gas responses for acetone were more than two times higher than those of the other gases. The dynamic change in acetone gas sensing was measured at the ppb and ppt levels at the optimal temperature. The variation in gas response with gas concentration from the ppt level to the ppm level is shown in Fig. S11.† It was confirmed that the gas response of the sensor was saturated at the ppm level. The results indicated that it is suitable for detection below ppb for our original purpose of skin gas detection. The dynamic curves clearly exhibited a resistance change according to acetone gas not only at the ppb level but also at the ppt level, as presented in Fig. 4c and d, respectively. To further evaluate the sensing performance of the ZnO nanobelts, the linearity of the response to variations in the concentration and the limit of detection (LOD) were analyzed (Fig. 4e and f). In the ppb range, the sensor response to variations in the gas concentration showed higher R^2 values for polynomial fits, indicating that the ZnO nanobelt sensor was saturated in the range of several hundred ppb. However, it showed good linearity in the ppt range ($R^2 = 0.995$), and its LOD was only 72 ppt. The LOD is equal to $3.3 \times \sigma/S$, where σ is the standard deviation of the blank signal, and S is the slope of the linear fit.[31] Therefore, the ZnO nanobelts are a reliable sensing material for a few hundred ppt to a few tens of ppb of acetone gas, and they are suitable for the analysis of acetone in skin gas.

Although our sensing material only comprised ZnO nanobelts as a pure metal oxide, its acetone gas sensing performance was superior to most previously reported results, which were obtained using p–n junctions or novel metal catalysts (Fig. 5a, Table S2†).[32–43] Moreover, this work has great value for practical measurements below ppt levels of acetone gas. As shown in Fig. 5b, several researchers reported theoretical LODs that were less than a few ppb, but their experimental LODs were over a few tens or hundreds of ppb. However, our gas sensing measurement was conducted up to 200 ppt, and its theoretical LOD was 72 ppt.

The unique structure of ZnO nanobelts with atomic level modification could lead to excellent sensing performance at extremely low acetone concentrations (ppt level). For further discussion, an understanding of the gas-sensing mechanism corresponding to the molecular reaction process on the surface is required. Gas sensing is performed by detecting a resistance change that occurs through the interaction between the pre-adsorbed oxygen species and the target gas molecules. Pre-adsorbed oxygen species are generated when the metal oxide is exposed to air at high temperatures. The state of oxygen is converted according to temperature as follows:

$$\mathrm{O_2(gas)} \leftrightarrow \mathrm{O_2(ad)} \leftrightarrow \mathrm{O_2^-(ad)} \leftrightarrow \mathrm{O^-(ad)} \leftrightarrow \mathrm{O^{2-}(ad)} \leftrightarrow \mathrm{O^{2-}(lattice)} \quad (1)$$

During oxygen adsorption on the surface, ZnO, as a typical n-type metal oxide semiconductor, generates a depletion layer by extracting electrons from the conduction band. The depletion layer induces a high potential barrier, and consequently, the resistance increases. Subsequently, the pre-adsorbed oxygen species on the surface are reduced by acetone molecules when they come into contact with the gas sensor. Acetone is converted to carbon dioxide and water as follows:

$$\mathrm{CH_3COCH_3 + 8O^-(ads) \rightarrow 3CO_2 + 3H_2O + 8e^-} \quad (2)$$

$$\mathrm{CH_3COCH_3 + O_2^-(ads) \rightarrow CH_3C^+O + CH_3O^- + e^-} \quad (3)$$

$$\mathrm{CH_3C^+O \rightarrow CH_3^+ + CO} \quad (4)$$

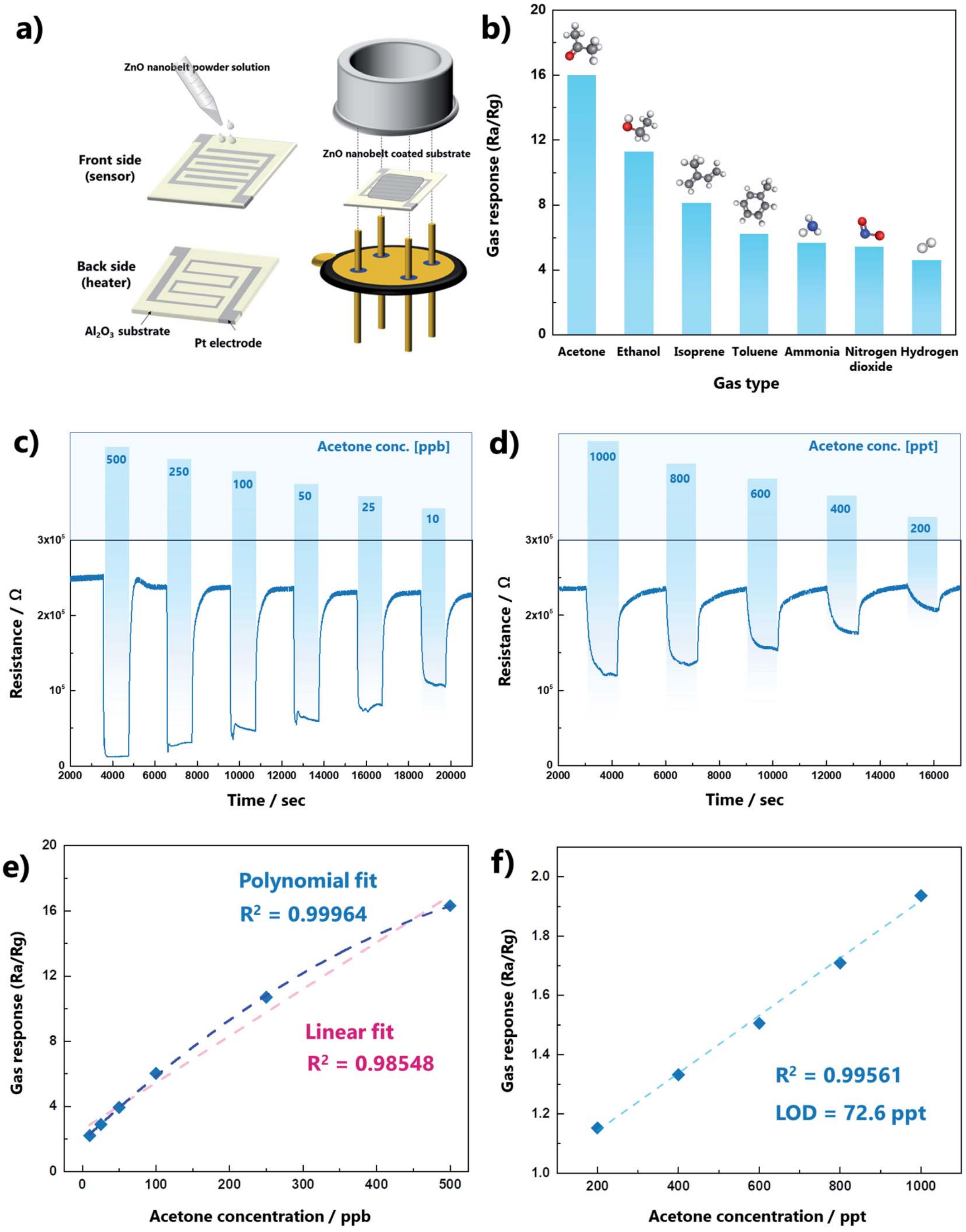

Fig. 4 (a) Schematic of gas sensor preparation using a porous ZnO nanobelt dispersion, (b) gas response with various types of gases at 500 ppb, and dynamic curves of acetone gas sensing for (c) ppb and (d) ppt levels, and the gas response for various acetone gas concentrations and their fitting results below (e) ppb and (f) ppt levels.

$$CO + O_2^-(ads) \rightarrow CO_2 + e^- \tag{5}$$

After these reactions, electrons trapped by the pre-adsorbed oxygen species are released back into the conduction band, and the potential barrier decreases. Therefore, gas sensing can be performed by measuring the variation in the resistance.

Based on this reaction mechanism, pre-adsorbed oxygen is considered a significant factor controlling the potential barrier for gas sensing. The magnitude of the resistance variation can be determined by the amount of pre-adsorbed oxygen that is formed and consumed on the surface. The atomic step structures enhance the generation of pre-adsorbed oxygen because of their high reactivity, as shown in Fig. 5c. The order of energies on a planar surface is $E_{\text{bulk}} < E_{\text{surface}} < E_{\text{step}} < E_{\text{kink}}$.[44] The difference in surface energy corresponding to coordinatively unsaturated sites at an edge is favorable for electron transfer. Thus, Zn atoms at the atomic step can easily react with an oxygen molecule, generating pre-adsorbed oxygen. Another role

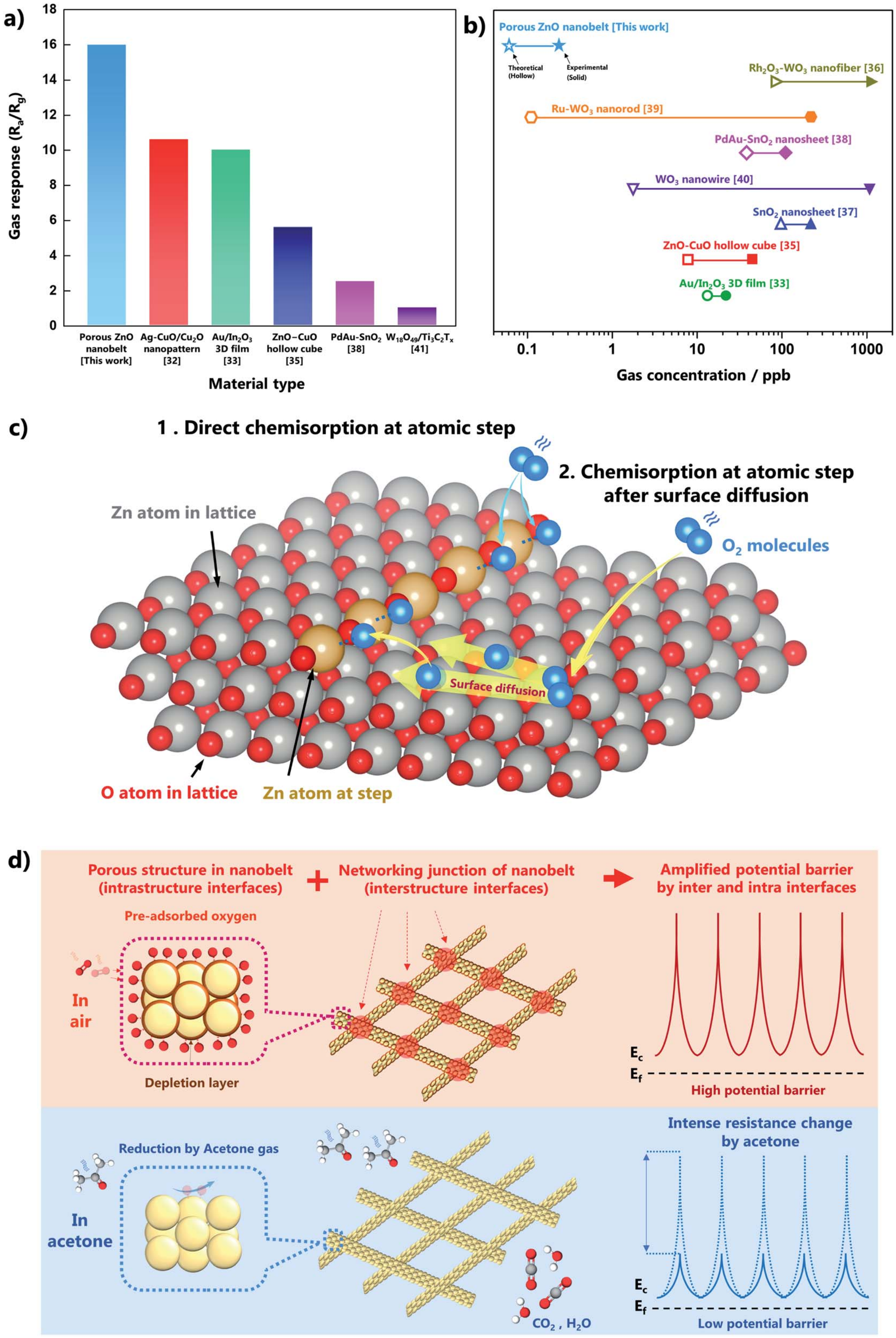

Fig. 5 (a) Comparison of the gas response of various acetone gas sensors at 500 ppb, (b) comparison of the experimental/theoretical LODs of various acetone gas sensors, (c) schematic of the advantages of the atomic step structure for oxygen chemisorption, and (d) schematic of the structural effect of porous nanobelts on the potential barrier.

of the atomic step structure is the restriction of the surface diffusion of oxygen atoms. Oxygen atoms can diffuse on the surface owing to their kinetic energy, and this movement may interrupt adsorption on the surface. However, the presence of a step structure can inhibit diffusion and induce the adsorption of oxygen species. Several density functional theory calculations have reported that the oxygen adsorption energy on a stepped structure is lower than that on a flat structure.[45–47] Therefore, the atomic step structure on the surface strongly improves the gas sensitivity.

In addition, the structural properties of the sensing material, such as porosity and one-dimensional structure, could enhance the sensitivity by amplifying the potential barrier due to the formation of the depletion layer. As presented in Fig. 5d, the porous structure provides numerous interfaces, and the belt structure also makes additional interfaces at the networking junctions. The large number of interfaces in the intra- and inter-structures leads to an intense change in the potential barriers. These mechanisms could provide a synergistic effect resulting in superior sensing performance, *i.e.,* detection of acetone variation at extremely low concentrations.

3. Conclusion

In this work, porous ZnO nanobelts with atomic step structures were successfully synthesized. The width of the nanobelts was less than 100 nm, and the length was several micrometers. Numerous uniformly distributed atomic step structures were observed on the ZnO surface as (100) facets. The sensor employing the ZnO nanobelts exhibited ultrahigh sensitivity, with a gas response of 16.5 at 500 ppb, and the experimental and theoretical LODs were 200 and 72 ppt, respectively. This result from a pure oxide was superior to competitive results obtained using metal catalysts or p–n junctions. The atomic step structures allow ultrahigh sensitivity owing to coordinatively unsaturated Zn sites and restricted surface diffusion. In addition, the amplified potential barrier due to the porous and 1D material structure produces a synergistic effect. Notably, the porous ZnO nanobelts can detect acetone in the ppt range with excellent linearity. Thus, they are an attractive candidate for reliable acetone gas sensors to detect small concentration changes in skin gas. Furthermore, through the development of an atomic level modification technique, a cost-effective catalyst-free gas sensor can be applied for real-time human condition monitoring by skin gas sensing.

4. Experimental section

4.1. Chemicals

Zinc fluoride tetrahydrate ($ZnF_2 \cdot 4H_2O$) and HMT were purchased from Wako Chemicals (Japan). Distilled water was prepared using a water purifier (WG203, Yamato).

4.2. Preparation of porous ZnO nanobelts

First, 300 mg of $ZnF_2 \cdot 4H_2O$ and 240 mg of HMT were dissolved in 200 mL of distilled water at 80 °C. The prepared solution was placed in polypropylene vessels and maintained at 80 °C for 3 h to synthesize ZnOHF nanobelts. The white powder (ZnOHF) was collected by centrifugation, washed with ethanol, and then dried at 80 °C. The ZnOHF nanobelts were converted to porous ZnO nanobelts by heat treatment at 500 °C for 2 h, during which the color of the powder changed from white to light yellow.

4.3. Characterization

The conversion temperature from ZnOHF to ZnO was evaluated using TGA (Q50, TA Instruments) in air at a heating rate of 10 °C min^{-1} from room temperature to 900 °C. FE-SEM (JSM-6335FM, JEOL) was performed to confirm the nanobelt structure, and the porous and atomic step structures were observed *via* a TEM and HR-TEM (Tecnai Osiris, FEI). The crystal structures of the samples were revealed *via* XRD (SmartLab, Rigaku Co., Ltd.) with Cu Kα ($\lambda = 1.5418$ Å) radiation at 40 kV and 30 mA; the diffraction patterns were acquired in the range 10–80°. The chemical state of the surface was investigated using XPS (ESCA 3400, Shimadzu). N_2 adsorption/desorption isotherms were obtained at 77 K (cooled by liquid nitrogen) using a surface area analyzer (Nova 2200e, Quantachrome Instruments), and the specific surface area was determined using the BET method. The crystal structure models were produced using the VESTA program.[48]

4.4. Acetone gas sensing measurements

A ZnO nanobelt gas sensor was prepared using a Pt-interdigitated electrode chip (3 × 3 mm) as the substrate. ZnO powder (10 mg) was mixed with ethanol (3 mL) and uniformly dispersed in an ultrasonic bath for 30 min. Subsequently, the solution (5 μL) was dropped onto the electrode chip and dried.

The sensing measurements were performed using a gas mixer (MU-3609, Horiba) and a resistance meter. The prepared gas sensor was installed in a chamber and detailed information of the chamber is presented in Fig. S12.† The working temperature was controlled in the range 450–550 °C. The variation in the temperature of the sensor with the applied voltage was measured using a thermal camera (T420, FLIR). Pretreatment was conducted at each working temperature for 2 h in air to stabilize the gas sensor. The total flow rate in the chamber was fixed at 200 sccm in all experiments. The gas response to acetone as a target gas was defined as R_a/R_g, where R_a and R_g are the electrical resistances under air and the target gas, respectively.

Conflicts of interest

There are no conflicts to declare.

Acknowledgements

This article is based on results obtained from a project, JPNP19005, commissioned by the New Energy and Industrial Technology Development Organization (NEDO).

References

1 X. Xiao, X. Liu, H. Zhao, D. Chen, F. Liu, J. Xiang, Z. Hu and Y. Li, *Adv. Mater.*, 2012, **24**, 5762–5766.
2 L. Hu, Q. Peng and Y. Li, *J. Am. Chem. Soc.*, 2008, **130**, 16136–16137.
3 C. Qin, B. Hou, J. Wang, Q. Wang, G. Wang, M. Yu, C. Chen, L. Jia and D. Li, *ACS Catal.*, 2018, **8**, 9447–9455.
4 Y. Lou, J. Liu, M. Liu and F. Wang, *ACS Catal.*, 2020, **10**, 2443–2451.
5 J. Y. Chen, C. W. Huang and W. W. Wu, *Small*, 2018, **14**, 1–8.
6 I. M. N. Groot, A. W. Kleyn and L. B. F. Juurlink, *Angew. Chem., Int. Ed.*, 2011, **50**, 5174–5177.
7 M. A. Petersen, J. A. Van Den Berg, I. M. Ciobîcă and P. Van Helden, *ACS Catal.*, 2017, **7**, 1984–1992.
8 Y. Nie, J. Pan, W. Zheng, J. Zhou and C. Q. Sun, *J. Phys. Chem. C*, 2011, **115**, 7450–7455.
9 H. S. Taylor, *Proc. R. Soc. A*, 1925, **28**, 105–111.
10 D. W. Blakely and G. A. Somorjai, *J. Catal.*, 1976, **42**, 181–196.
11 S. Dahl, A. Logadottir, R. C. Egeberg, J. H. Larsen, I. Chorkendorff, E. Törnqvist and J. K. Nørskov, *Phys. Rev. Lett.*, 1999, **83**, 1814–1817.
12 M. Urdea, L. A. Penny, S. S. Olmsted, M. Y. Giovanni, P. Kaspar, A. Shepherd, P. Wilson, C. A. Dahl, S. Buchsbaum, G. Moeller and D. C. Hay Burgess, *Nature*, 2006, **444**, 73–79.
13 S. T. Krishnan, J. P. Devadhasan and S. Kim, *Anal. Bioanal. Chem.*, 2017, **409**, 21–31.
14 T. A. Popov, *Ann. Allergy, Asthma, Immunol.*, 2011, **106**, 451–456.
15 G. Freund, *Metabolism*, 1965, **14**, 985–990.
16 V. Ruzsányi and M. P. Kalapos, *J. Breath Res.*, 2017, **11**, 024002.
17 M. Ye, P. J. Chien, K. Toma, T. Arakawa and K. Mitsubayashi, *Biosens. Bioelectron.*, 2015, **73**, 208–213.
18 T. Arakawa, T. Suzuki, M. Tsujii, K. Iitani, P. Chien and M. Ye, *Biosens. Bioelectron.*, 2019, **129**, 245–253.
19 P. Mochalski, J. King, K. Unterkofler, H. Hinterhuber and A. Amann, *J. Chromatogr. B*, 2014, **959**, 62–70.
20 T. Arakawa, T. Aota, K. Iitani, K. Toma, Y. Iwasaki and K. Mitsubayashi, *Talanta*, 2020, **219**, 121187.
21 M. E. Hair, R. Gerkman, A. I. Mathis and L. Hala, *Anal. Chem.*, 2019, **91**, 15860–15865.
22 J. C. Anderson, *Obesity*, 2015, **23**, 2327–2334.
23 N. Yamane, T. Tsuda, K. Nose, A. Yamamoto, H. Ishiguro and T. Kondo, *Clin. Chim. Acta*, 2006, **365**, 325–329.
24 Y. Sekine, S. Toyooka and S. F. Watts, *J. Chromatogr. B: Anal. Technol. Biomed. Life Sci.*, 2007, **859**, 201–207.
25 E. A. Secco, *Can. J. Chem.*, 1967, **45**, 585–588.
26 X. Zheng, H. Fan, H. Wang, B. Yan, J. Ma, W. Wang, A. K. Yadav, W. Dong and S. Wang, *Ceram. Int.*, 2020, **46**, 27499–27507.
27 T. Kawabe, K. Tabata, E. Suzuki, Y. Yamaguchi and Y. Nagasawa, *J. Phys. Chem. B*, 2001, **105**, 4239–4244.
28 Y. Zhang, Y. Zhao, T. Otroshchenko, H. Lund, M. M. Pohl, U. Rodemerck, D. Linke, H. Jiao, G. Jiang and E. V. Kondratenko, *Nat. Commun.*, 2018, **9**, 1–10.
29 K. Kim, P. G. Choi, T. Itoh and Y. Masuda, *Adv. Mater. Interfaces*, 2021, **8**, 2100283.
30 L. Ahrem, G. Scholz, T. Gutmann, B. Calvo, G. Buntkowsky and E. Kemnitz, *J. Phys. Chem. C*, 2017, **121**, 12206–12213.
31 A. D. McNaught and A. Wilkinson, *IUPAC Compendium of Chemical Terminology*, 1997, p. 3540.
32 Y. M. Choi, S. Y. Cho, D. Jang, H. J. Koh, J. Choi, C. H. Kim and H. T. Jung, *Adv. Funct. Mater.*, 2019, **29**, 1–9.
33 R. Xing, Q. Li, L. Xia, J. Song, L. Xu, J. Zhang, Y. Xie and H. Song, *Nanoscale*, 2015, **7**, 13051–13060.
34 W. Liu, Y. Xie, T. Chen, Q. Lu, S. Ur Rehman and L. Zhu, *Sens. Actuators, B*, 2019, **298**, 126871.
35 J. E. Lee, C. K. Lim, H. J. Park, H. Song, S. Y. Choi and D. S. Lee, *ACS Appl. Mater. Interfaces*, 2020, **12**, 35688–35697.
36 N. H. Kim, S. J. Choi, S. J. Kim, H. J. Cho, J. S. Jang, W. T. Koo, M. Kim and I. D. Kim, *Sens. Actuators, B*, 2016, **224**, 185–192.
37 K. Kim, P. G. Choi, T. Itoh and Y. Masuda, *ACS Appl. Mater. Interfaces*, 2020, **12**, 51637–51644.
38 G. Li, Z. Cheng, Q. Xiang, L. Yan, X. Wang and J. Xu, *Sens. Actuators, B*, 2019, **283**, 590–601.
39 Y. G. Song, J. Y. Park, J. M. Suh, Y. S. Shim, S. Y. Yi, H. W. Jang, S. Kim, J. M. Yuk, B. K. Ju and C. Y. Kang, *Chem. Mater.*, 2019, **31**, 207–215.
40 K. Yuan, C. Y. Wang, L. Y. Zhu, Q. Cao, J. H. Yang, X. X. Li, W. Huang, Y. Y. Wang, H. L. Lu and D. W. Zhang, *ACS Appl. Mater. Interfaces*, 2020, **12**, 14095–14104.
41 W. Zhang, Y. Fan, T. Yuan, B. Lu, Y. Liu, Z. Li, G. Li, Z. Cheng and J. Xu, *ACS Appl. Mater. Interfaces*, 2020, **12**, 3755–3763.
42 X. Chang, X. Li, X. Qiao, K. Li, Y. Xiong, X. Li, T. Guo, L. Zhu and Q. Xue, *Sens. Actuators, B*, 2020, **304**, 127430.
43 X. Chang, X. Qiao, K. Li, P. Wang, Y. Xiong, X. Li, F. Xia and Q. Xue, *Sens. Actuators, B*, 2020, **317**, 128208.
44 L. V. Goncharova, *Basic Surfaces and Their Analysis*, 2018, pp. 2–14.
45 K. Cao, R. van Lent, A. W. Kleyn, M. Kurahashi and L. B. F. Juurlink, *Proc. Natl. Acad. Sci. U. S. A.*, 2019, **116**, 13862–13866.
46 T. Ogawa, A. Kuwabara, C. A. J. Fisher, H. Moriwake and T. Miwa, *J. Phys. Chem. C*, 2013, **117**, 9772–9778.
47 T. A. Baker, C. M. Friend and E. Kaxiras, *J. Phys. Chem. C*, 2009, **113**, 3232–3238.
48 K. Momma and F. Izumi, *J. Appl. Crystallogr.*, 2008, **41**, 653–658.